Progress In Electromagnetics Research C, Vol. 96, 179–192, 2019

SOSM Direct Torque and Direct Suspension Force Control for Double Stator Bearingless Switched Reluctance Motor

Chu Chen*, Huijie Guo, and Ge Zhang

Abstract—Because of the current commutation and the double salient pole structure of bearingless switched reluctance motors (BSRMs), the torque and suspension force have large ripples when traditional current control methods are used. According to the special structure of the double stator BSRM (DSBSRM), the direct decoupling of torque and suspension force is realized. Therefore, the DSBSRM can be controlled separately as a conventional 12/8 SRM and a four-poles active magnetic bearing. In order to achieve the suppression of the torque ripple and improve the robustness of speed, a direct torque control (DTC) strategy using second order sliding mode (SOSM) speed controller is proposed. In order to achieve the suppression of the suspension force ripple and rotor displacement chattering, a direct suspension force control (DSFC) strategy is proposed as well. Then the SOSM-DT/DSFC model is established by simulink. The results of simulation show that the torque ripple, suspension force ripple, and rotor radial displacements of DSBSRM can be reduced respectively. Moreover, the proposed control strategy has better robustness and dynamic performance than traditional control strategy.

1. INTRODUCTION

Switched reluctance motors (SRMs) are characterized by having high starting torque, simple and robust structure, low cost, inherent fault tolerance, and no rotor windings [1–3]. These features make the SRM attractive for electric vehicles and aeronautical applications [4, 5]. In order to avoid the mechanical friction between the shaft and bearing, the bearingless switched reluctance motor (BSRM) was developed by Takemoto et al. which can achieve rotation and suspension in the same motor [6]. Therefore, BSRM has the advantages of low mechanical loss and high critical speed, and has great application prospects in the field of flywheel energy storage system and superconducting maglev trains [7]. However, there is a nonlinear strong coupling relationship between torque windings and suspension windings in BSRM, which leads to the complexity of decoupling control [8, 9].

In recent years, some scholars have tried to weaken the coupling between windings from the point of view of motor structure design and studied several novel BSRM topology structures, including hybrid stator BSRM, double stator BSRM, and width stator BSRM [10–13]. Reference [10] proposed a 8/10 hybrid stator type BSRM. The stator poles are designed with wide and narrow poles. The suspension windings are superimposed on the wide pole teeth, and the torque windings are superimposed on the narrow pole teeth, which reduces the coupling between torque and suspension. Based on the 8/10 hybrid stator BSRM, a new 12/14 hybrid stator BSRM structure was presented in [11]. Reference [12] proposed a novel width rotor BSRM. The width rotor BSRM divides inductance into suspension and torque intervals, thereby achieving the decoupling of torque and suspension. Reference [13] proposed a new structure of double stator BSRM (DSBSRM). The suspension and torque windings are respectively

Received 12 July 2019, Accepted 28 September 2019, Scheduled 2 November 2019
* Corresponding author: Chu Chen (609664765@qq.com).
The authors are with the School of Electrical and Power Engineering, China University of Mining and Technology, Xuzhou 221116, China.

on the inner and outer stators of DSBSRM, and the two sets of windings have independent magnetic flux paths, which effectively overcome the coupling between suspension force and torque.

However, because of the double-salient-pole structure and pulse-type phase currents, that large ripples exist in the radial force and torque has been the significant shortcoming which restricts BSRMs' application [14, 15]. Hence, it is necessary to study its low torque ripple and low suspension force ripple operation. In 1980s, the concept of DTC was proposed for AC motor drives, which is a simple solution to facilitate the torque control and decrease the torque ripple of AC motors by regulating the flux as a constant [16]. Based on the DTC of conventional AC motors, the DTC of SRMs was firstly proposed as a solution of sensorless for SRM drives, which requires the change of the winding configuration, bipolar currents and short-path flux patterns [17]. In [18], a traditional square wave current control method for 12/8 BSRM was proposed. In [19], a torque and suspension force decoupling control method was proposed. In [20], an average torque and suspension force independent control strategy was proposed. In [21], a suspension force square-wave current control strategy which can reduce the coupling of suspension forces in x and y directions for width rotor teeth BSRM was presented. When the parameters of the motor system change, the traditional PID control can no longer meet the high-performance operation requirements. High-order sliding mode control has the characteristics of fast response, insensitivity to disturbance and parameter change, and simple implementation. It is widely used in motor control [22–25]. In [22], high-order sliding mode control is applied to the nonlinear control of induction motor, which improves the static and dynamic performance of motor speed regulation and enhances the robustness. In [23], the chattering problem in PMSM control system is effectively eliminated by using high-order sliding mode. In [24], for the SRM torque ripple problem, a high-order sliding mode is used to reduce the chattering of the output speed.

For the purpose of simultaneously achieving the suppression of the torque and suspension force ripple of DSBSRM, a direct torque and direct suspension force control (DT/DSFC) strategy is proposed in this paper. The control system is divided into two parts: torque subsystem and suspension force subsystem. Firstly, the structure and operating principle of DSBSRM are introduced. Then, the mathematical model of DSBSRM and DT/DSFC principle are given. In order to further reduce the chattering of output speed and enhance the robustness of the torque subsystem, a second order sliding mode (SOSM) controller using super-twisting algorithm is designed. Finally, the effectiveness of the SOSM-DT/DSFC method is validated by simulink.

2. TOPOLOGY AND MATHEMATICAL MODEL OF DSBSRM

2.1. Topology Structure of DSBSRM

As shown in Figure 1, a DSBSRM mainly comprises an outer stator with 12 poles, a rotor with 8 poles, and an inner stator with 4 poles. The torque stator is outside, which mainly produces rotational torque. The radial force stator is inside, which mainly generates radial force to suspend rotor. Torque windings and suspension force windings have independent magnetic flux paths, which effectively solves the coupling problem between the motor rotation function and suspension function, and simplifies the control difficulty of the system. Windings on pole A1, pole A2, pole A3, and pole A4 are connected in series to construct torque winding A. Windings on radial force pole such as P1, P2, P3, and P4 are independently controlled to construct four radial force windings in x and y directions.

The decoupling characteristics of the DSBSRM torque subsystem and suspension subsystem can be proved by [13]. Therefore, the DSBSRM can be controlled separately as a conventional 12/8 SRM and a four-poles active magnetic bearing.

2.2. Mathematical Model

The torque expression of DSBSRM can be expressed as Eq. (1).

$$T_e = i_m \frac{d\psi_k(\theta, i_m)}{d\theta} \tag{1}$$

here, i_m is the torque winding current; ψ_k is the stator flux linkage; θ is the rotor position angle.

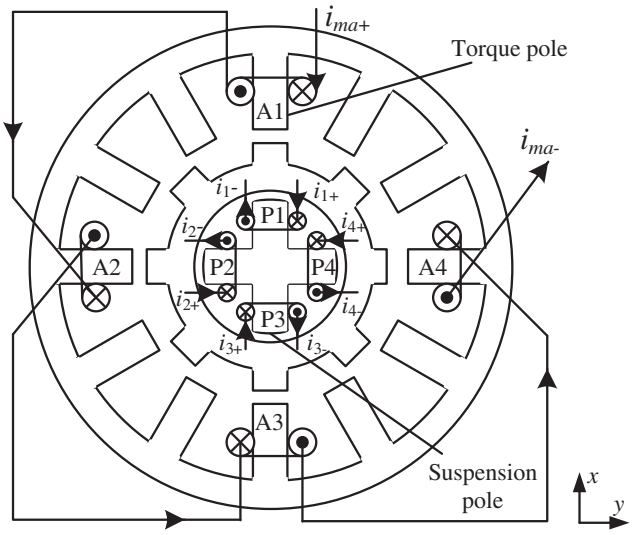

Figure 1. Structure of DSBSRM.

Assuming that the eccentricities of the rotor in the positive direction of x-axis and y-axis are x and y respectively, and ignoring the effect of magnetic saturation of the suspension pole, the suspension force produced by i_{x1}, i_{y1}, i_{x2}, and i_{y2} can be derived from the virtual displacement method:

$$F_{ij} = \frac{\mu_0 h \beta_r N_s^2 i_{ij}^2}{\left(2l_{ij}^2\right)}, \quad i = x, y;\ j = 1, 2 \tag{2}$$

In the above formula, μ_0 is the vacuum permeability; h is the length of the laminations; r is the radius of the inner stator; β_r is the tooth width of the inner stator, and its value is $\pi r/4$.

In addition,

$$\begin{cases} l_{x1} = g_2 - x \\ l_{y1} = g_2 - y \\ l_{x2} = g_2 + x \\ l_{y1} = g_2 + y \end{cases} \tag{3}$$

here, g_2 is the air gap length between inner stator and rotor of DSBSRM.

3. DSBSRMSOSM-DT/DSFC STRATEGY

3.1. Principle of DTC Scheme

Due to formula (1), there is a first order delay link between torque winding current and flux linkage, and torque can be controlled only by changing flux. The positive and negative of the instantaneous electromagnetic torque T_e can be changed by changing the positive and negative of ψ_k.

According to the voltage balance equation, the torque winding voltage U_k can be expressed as Eq. (4).

$$U_k = R_k i_k + \frac{d\psi_k}{d_t} \tag{4}$$

where $R_k i_k$ is the stator resistance voltage drop, and it can be neglected because $R_k i_k$ is far less than U_k. So, the expression of ψ_k can be obtained as follows:

$$\psi_k = \int U_k d_t \tag{5}$$

Discretization of Eq. (5) can be achieved:

$$\psi_k = \psi_{k-1} + U_k \Delta t \tag{6}$$

Therefore, the stator flux amplitude can be controlled by choosing the appropriate space voltage vector relationship.

There is almost no coupling between the torque and the suspension force of DSBSRM, so the magnitude and angle of flux can be controlled by choosing the space voltage vector of the torque to achieve the purpose of controlling the torque. The three-phase asymmetric half-bridge structure is chosen as the torque winding power conversion circuit. We can give the following three voltage states: state 1, state 0, state -1. State 1 indicates that the phase torque voltage is forward conducting; state 0 indicates that the phase torque voltage is zero; and state -1 indicates that the phase torque voltage is reversed. Considering the normal operation and working efficiency of the motor, six space voltage vectors of torque windings, $U_1, U_2, U_3, U_4, U_5, U_6$, are determined. There are six connected stats for six different voltage space vectors: $U_1(1, 0, -1)$, $U_2(0, 1, -1)$, $U_2(-1, 1, 0)$, $U_4(-1, 0, 1)$, $U_5(0, -1, 1)$ and $U_6(1, -1, 0)$. Figure 2 shows the equivalent space voltage vector of DSBSRM.

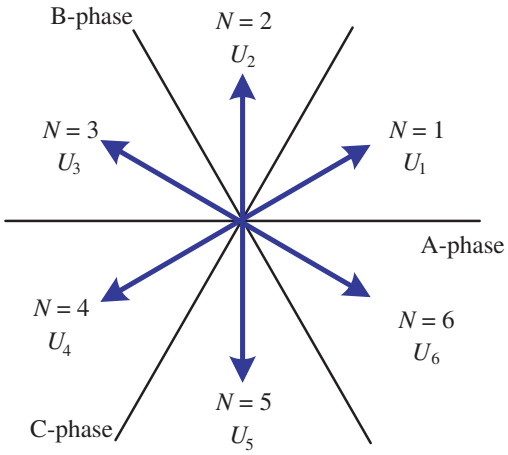

Figure 2. Equivalent space voltage vector of DSBSRM.

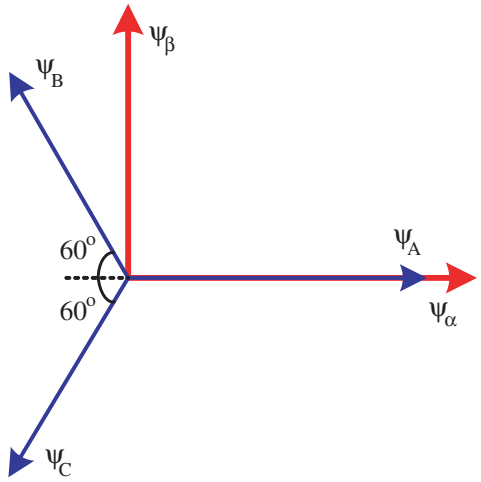

Figure 3. Flux vector diagram of DSBSRM.

Table 1 shows the switching states corresponding to the torque voltage space vector of DSBSRM.

In order to simplify the estimation of flux linkage and its angle, this paper uses the coordinate transformation method to combine the independent three-phase flux linkages in DSBSRM, as shown in Figure 3.

According to the coordinate transformation method as shown in Figure 3, the positive direction of phase-A axis is overlapped with the α axis of the vector complex plane. Thus, the magnetic fluxes in

Table 1. Equivalent space voltage vector state table.

Space voltage vector	U_{ma}, U_{mb}, U_{mc}
U_1	$(1, 0, -1)$
U_2	$(0, 1, -1)$
U_3	$(-1, 1, 0)$
U_4	$(-1, 0, 1)$
U_5	$(0, -1, 1)$
U_6	$(1, -1, 0)$

the α and β directions can be obtained:

$$\begin{cases} \psi_\alpha = \psi_A - \psi_B \cos\dfrac{\pi}{3} - \psi_C \cos\frac{\pi}{3} \\ \psi_\beta = \psi_B \sin\dfrac{\pi}{3} - \psi_C \sin\frac{\pi}{3} \end{cases} \tag{7}$$

As a result, the magnitude and phase of synthesis flux linkage can be calculated by Eqs. (8) and (9).

$$\psi = \sqrt{\psi_\alpha^2 + \psi_\beta^2} \tag{8}$$

$$\delta = \arctan 2\left(\frac{\psi_\beta}{\psi_\alpha}\right) \tag{9}$$

According to the torque winding current of DSBSRM, hysteresis loops are compared between real-time torque T and estimated torque T^*, and hysteresis loops are compared between real-time flux ψ and estimated flux ψ^*. The equivalent space voltage vector of DSBSRM is selected, as shown in Table 2. The symbols $\uparrow$ and $\downarrow$ represent the increase and decrease of torque or flux linkage, respectively.

Table 2. Equivalent space voltage vector switch table.

$T\uparrow\psi\uparrow$	$T\uparrow\psi\uparrow$	$T\downarrow\psi\uparrow$	$T\downarrow\psi\downarrow$
U_{N+1}	U_{N+2}	U_{N-1}	U_{N-2}

3.2. SOSM-DTC Scheme

The high-order sliding mode has the characteristics of fast response, suppression of chattering, high control precision, and strong robustness in the motion control system. In order to further reduce the chattering of the output speed, enhance the robustness of the speed, and improve the dynamic response capability of the speed, the super-twisting algorithm is used to design the second-order sliding mode control in the torque subsystem of DSBSRM DT/DSFC.

3.2.1. Principle of SOSM

Considering that DSBSRM is a single input uncertain nonlinear system, formula (10) can be obtained.

$$\begin{cases} \dot{x} = f(x) + g(x)\,u \\ y = s(x,t) \end{cases} \tag{10}$$

here, x is the system state variable; u is the input quantity; $f(x)$ and $g(x)$ are smooth uncertain functions; $s(x,t)$ is the sliding mode variable. The super-twisting algorithm control law $u(t)$ consists of two parts, defined by continuous functions of discontinuous time derivatives and sliding mode variables.

$$u(t) = u_1(t) + v(t) \tag{11}$$

$$u_1(t) = \begin{cases} -\lambda_1 |S_0|^p \operatorname{sign}(s) & |S| > S_0 \\ -\lambda_1 |S|^p \operatorname{sign}(s) & |S| \le S_0 \end{cases} \tag{12}$$

$$\dot{v}(t) = \begin{cases} -u & |u| > 1 \\ -\dfrac{\lambda_2}{2}\operatorname{sign}(s) & |u| \le 1 \end{cases} \tag{13}$$

3.2.2. SOSM-Speed Controller Design

The torque expression of DSBSRM can be expressed as Eq. (14) when considering system load and friction loss in operating process.

$$T_e - T_L - \Im\omega = J\frac{d\omega}{dt} \tag{14}$$

here, $\Im$ is the friction coefficient; ω is the motor angular velocity.

In the torque subsystem of DSBSRM, speed outer loop, torque closed loop, and flux closed loop control are adopted. SOSM speed controller is used in the outer loop of speed, which makes the angular velocity track itself in real time. Speed state error is expressed as follows:

$$e = \omega - \omega^* \tag{15}$$

In order to simplify the controller design, the DSBSRM speed segment can be converted into the following form:

$$\dot{x} = u + d \tag{16}$$

here, $u = \frac{T_e}{J}$ and $d = -\frac{1}{J}(T_L + \Im\omega)$.

Selecting the sliding surface as $s = e$, the DSBSRM speed controller designed with the super-twisting algorithm is:

$$\begin{cases} T_e = J\left[\lambda_1 |s|^{1/2} \operatorname{sgn}(s) - Z\right] \\ \dot{Z} = -\lambda_2 \operatorname{sgn}(s) \end{cases} \tag{17}$$

By solving the derivative of the sliding mode variable in the above formula, the closed-loop system equation is obtained as follows:

$$\dot{z} = \begin{bmatrix} \dot{Z}_1 \\ \dot{Z}_2 \end{bmatrix} = \begin{bmatrix} -\lambda_1 |Z_1|^{1/2} \operatorname{sgn}(Z_1) + Z_2 + \delta \\ -\lambda_2 \operatorname{sgn}(Z_1) \end{bmatrix} \tag{18}$$

here, $Z_1 = s$, $z = \begin{bmatrix} Z_1 & Z_2 \end{bmatrix}^T$ and δ is the interference phase.

Therefore, the SOSM controller of DSBSRM torque subsystem can be designed as:

$$T_e = J\left(-\lambda_1 |\omega - \omega^*|^{1/2} \operatorname{sign}(\omega - \omega^*) - \int \frac{\lambda_2}{2} \operatorname{sign}(\omega - \omega^*)\, d(\omega - \omega^*)\right) \tag{19}$$

3.3. Principle of DSFC Scheme

For the closed-loop control of suspension force, the suspension force needs to be observed first. The estimation of suspension force can be calculated by Equation (2). At the same time, a two-point suspension force regulator is used to achieve high dynamics of the rotor suspension control of DSBSRM.

As shown in Figure 4, F_g is the given value of suspension force, F_f the feedback value of suspension force, and ΔF the error of F_g and F_f. ΔF is also the input of the suspension force regulator, F_Q the switching signal of the suspension windings and the output of the regulator, and $\pm\varepsilon_m$ the tolerance of the two-point suspension force regulator. The specific adjustment process of the suspension force is shown in Figure 5.

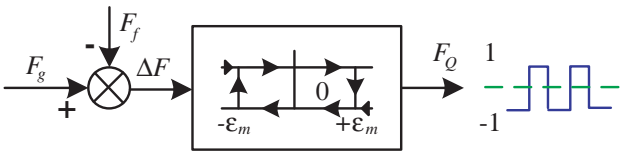

Figure 4. Bang-Bang controller of DSFC.

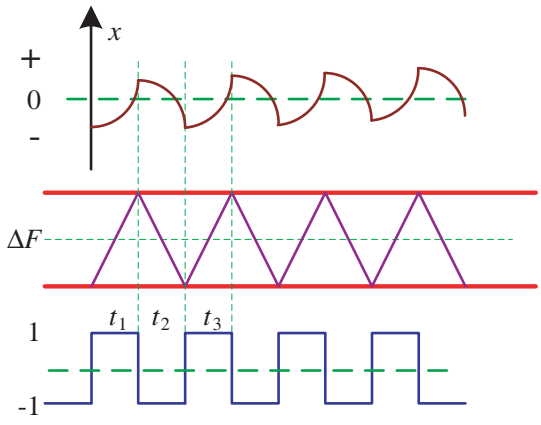

Figure 5. Suspension force adjustment principle of DSFC.

As shown in Figure 5, take the displacement direction of x-axis as an example. At time t_1, assume that the rotor is eccentric in the positive direction of the x-axis, and the error value of the suspension force is smaller than the lower tolerance limit $-\varepsilon_m$ set by the regulator. The suspension force controller will output -1, then the corresponding suspension force windings are reversed. At this time, the radial force of the rotor is increased in the negative direction of the x-axis to control the displacement of the rotor to the center. At time t_2, the rotor is eccentric in the negative direction, and the error value of the suspension force is larger than the upper tolerance limit $+\varepsilon_m$. The suspension force controller will output 1, then the corresponding suspension force windings are forward conducting. At this time, the radial force of the rotor is increased in the positive direction of the x-axis. Similarly, the process of adjusting the displacement of the rotor in the y-axis direction is the same.

It can be seen that the fluctuation of radial suspension force can be suppressed within the allowable tolerance range by reasonably choosing the tolerance limit of the regulator. Finally, the stable suspension of the rotor is realized.

3.4. Control Block of DSBSRMSOSM-DT/DSFC

Figure 6 shows the system control block of DSBSRM SOSM-DT/DSFC. This paper chooses a three-phase asymmetric half-bridge circuit as the torque winding power converter, and four-phase asymmetric half-bridge circuit as the suspension force winding power converter of DSBSRM. The torque subsystem adopts double closed-loop control. The outer loop is speed loop, and inner loop is torque loop and flux loop. The suspension subsystem adopts the closed-loop control of suspension force.

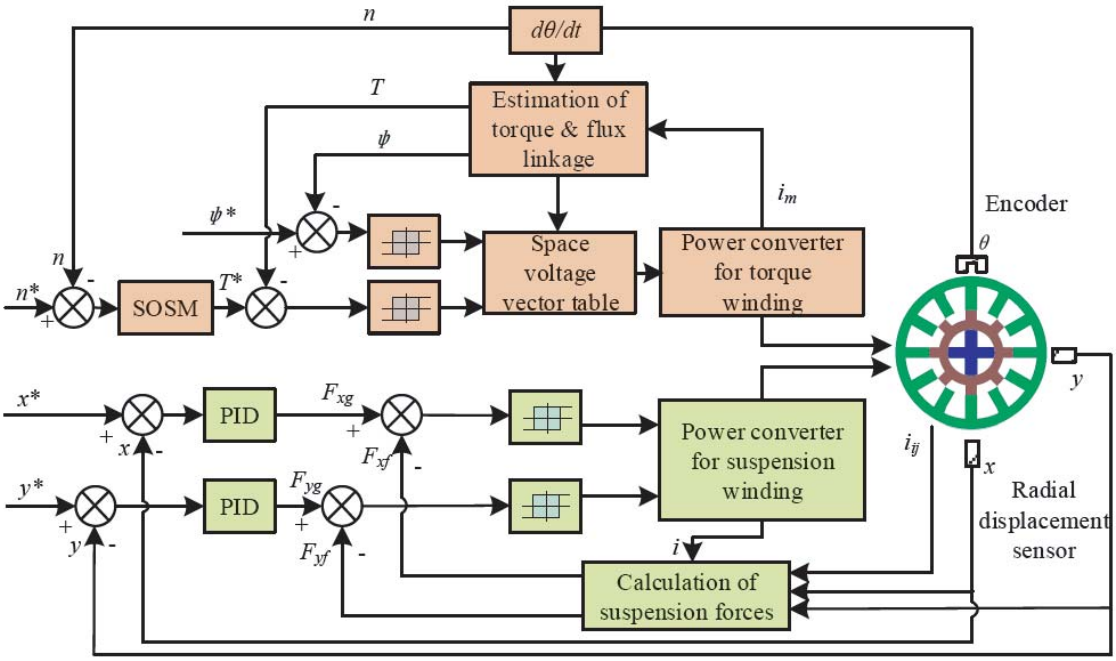

Figure 6. Control block of SOSM-DT/DSFC.

For the torque subsystem, $n*$ is the given speed, n the real-time speed, and Δn the difference between $n*$ and n. Δn is calculated by SOSM controller to get the given torque $T*$, and the deviation values of $T*$ and the estimated torque T based on real-time torque windings current are obtained by the hysteresis loop comparator to obtain the torque hysteresis signal. The deviation value of the given flux ψ^* and the estimated flux ψ are obtained by the hysteresis loop comparator to obtain the flux hysteresis signal. The torque and flux hysteresis signals are used as input signals for logic judgment of switching signal, and then a suitable space voltage vector is selected. Finally, the motor torque subsystem is controlled by the torque winding power converter.

For the suspension force subsystem, $x*$ and $y*$ are the given displacements; x and y are the real-time axial displacements; F_{xg} and F_{yg} are the given suspension forces; F_{xf} and F_{yf} are the real-time radial suspension forces of the rotor. The displacement errors $x*$-x and $y*$-y are generated by the PID regulator to generate the given suspension force F_{xg} and F_{yg}. The suspension force error is output by the suspension force two-point regulator to output the switching signal of suspension windings. The conduction phase of suspension windings is selected according to the rotor position signal. Finally, the suspension subsystem of DSBSRM is controlled by the suspension force power converter.

4. SIMULATION RESULTS AND DISCUSSIONS

According to the motor control block and mathematical model, the motor simulation model is established in Simulink. The parameters of the model are as follows: the given target speed is 2500 r/min; the load torque is 0.3 N·m; the flux hysteresis width is 0.001 Wb; the suspension force hysteresis width is 0.1 N; the torque hysteresis width is 0.1 N·m; and the simulation time is 20 seconds.

4.1. Simulation and Analysis of DT/DSFC and Traditional Square Wave Control

Figure 7 shows the flux-linkage trajectory at the speed of 2500 r/min with different control methods. It can be seen that the flux-linkage trajectory is of circular shape when using DT/DSFC method whereas that is of triangular diamond shape when using traditional square wave control method. Compared with the trianglar diamond, the circle can keep the magnitude of the flux basically constant. It can be seen that DT/DSFC strategy can effectively control the flux linkage amplitude of DSBSRM, so as to achieve the purpose of suppressing the torque ripple.

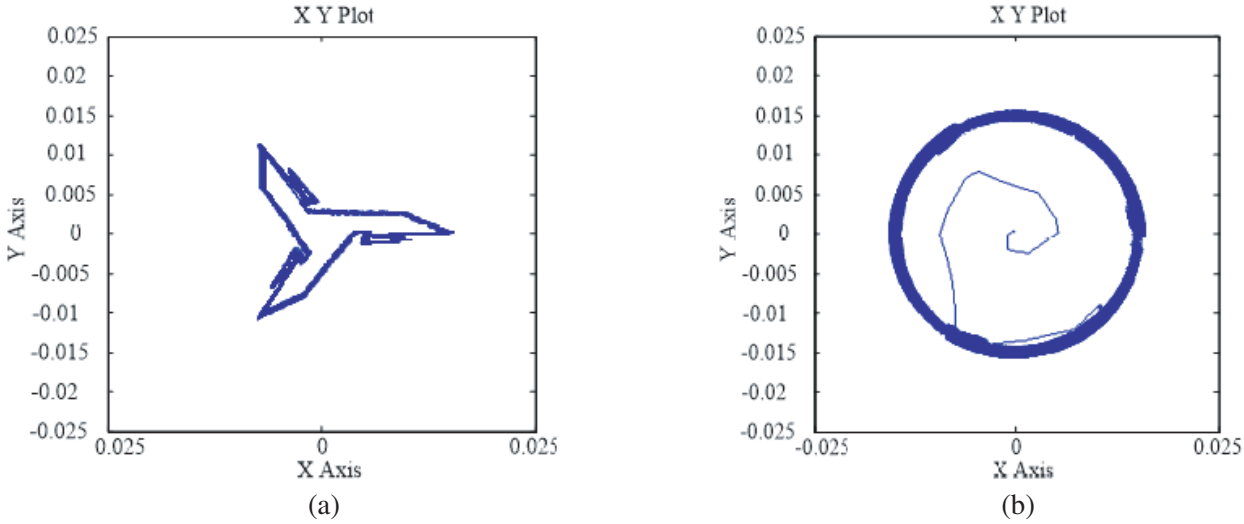

Figure 7. Flux linkage trajectory of DSBSRM. (a) Traditional square wave control. (b) DT/DSFC.

Figure 8 shows the torque ripple waveforms with different control methods. With the traditional square control method, the range of steady-state torque is $-0.1 \sim 0.45$ N·m, and the amplitude of the ripple is 0.55 N·m. With the DT/DSFC method, the range of steady-state torque is $0.2 \sim 0.4$ N·m, and the amplitude of the ripple is 0.2 N·m. It can be seen that DT/DSFC method reduces torque ripple by 75% compared with traditional square wave control method.

Figure 9 shows the suspension force ripple waveforms with different control methods. With the traditional square control method, the range of steady-state suspension force in x-axis is $-9 \sim 10$ N, and the amplitude of the ripple is 19 N. With the DT/DSFC method, the range of steady-state suspension force in x-axis is $-4 \sim 5$ N, and the amplitude of the ripple is 9 N. It can be seen that DT/DSFC method reduces suspension force ripple in x-axis by 52.6% compared with traditional square wave control

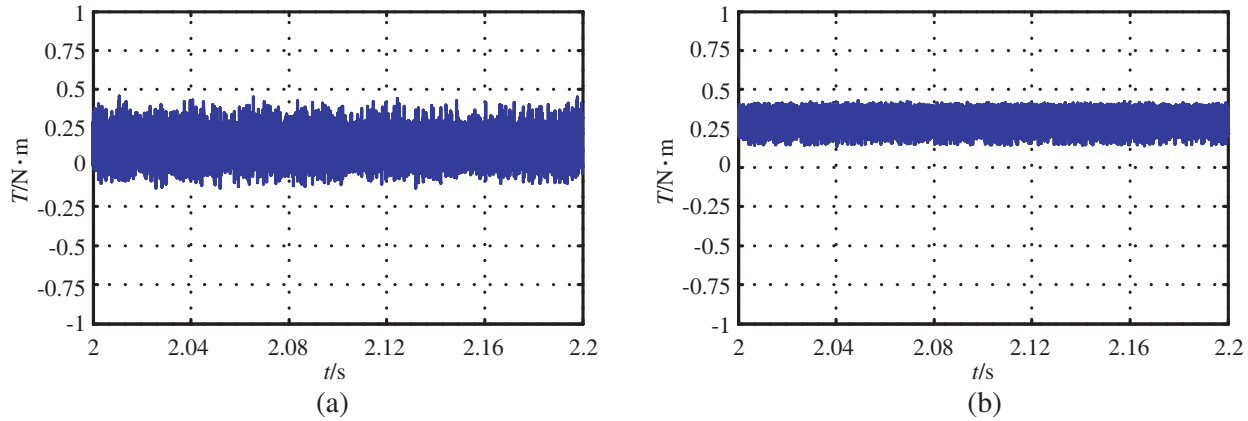

Figure 8. Torque ripple waveforms of DSBSRM. (a) Traditional square wave control. (b) DT/DSFC.

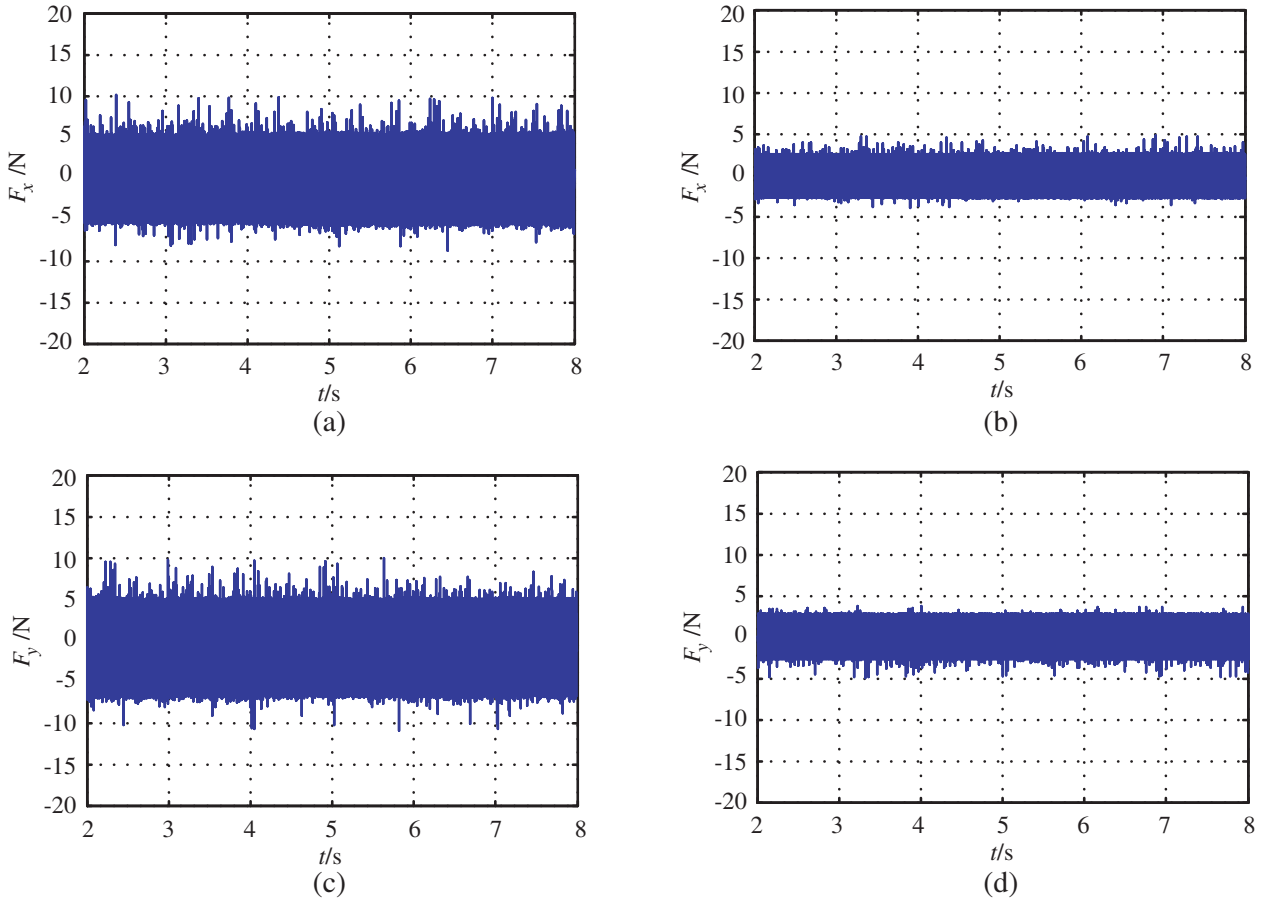

Figure 9. Suspension force ripple waveforms of DSBSRM. (a) x-axis with traditional square wave control. (b) x-axis withDT/DSFC. (c) y-axis with traditional square wave control. (d) y-axis with DT/DSFC.

method. Similarly, DT/DSFC method reduces suspension force ripple in y-axis by 55% compared with traditional square wave control method.

Figure 10 shows the rotor displacement waveforms in x axis with different control methods. With the traditional square control method, the range of rotor displacement in x-axis is $-0.1 \sim 0.11$ mm, and

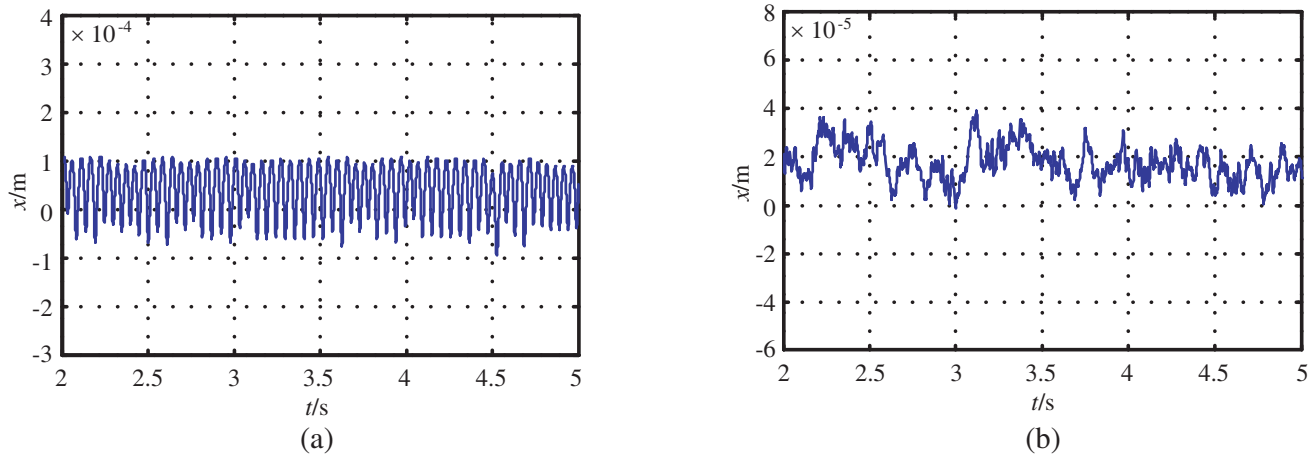

Figure 10. Rotor displacement in x axis of DSBSRM. (a) Traditional square wave control. (b) DT/DSFC.

the amplitude of the ripple is 0.21 mm. With the DT/DSFC method, the range of rotor displacement is $0 \sim 0.05$ mm, and the amplitude of the ripple is 0.05 mm. It can be seen that DT/DSFC method reduces the amplitude of rotor displacement by 76.2% and the maximum displacement error by 54.5% in x-axis compared with traditional square wave control method.

4.2. Simulation and Analysis of SOSM-DT/DSFC and DT/DSFC

Figure 11 shows the change in speed of the square wave control, DT/DSFCand SOSM-DT/DSFC when motor starts. The speed of the traditional square wave control method reaches the steady state at 2.2 s. And the DT/DSFC method reaches the target speed at 1.5 s, which is 40% faster than the square wave control strategy. SOSM-DT/DSFC method rises to the target speed in 1 s, and there is basically no overshoot. Therefore, the dynamic response speed of SOSM-DT/DSFC method is increased by 60% compared with the traditional square wave control method and by 32% compared with DT/DSFC method.

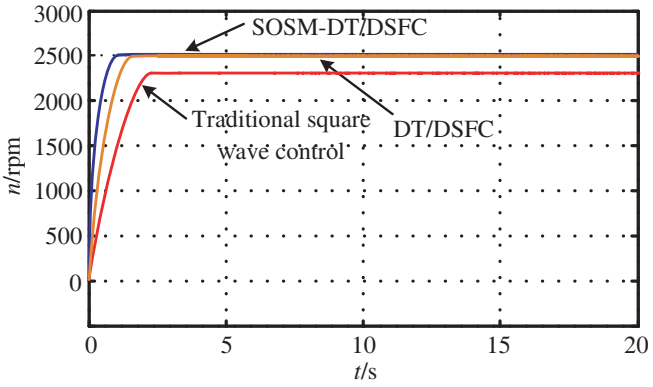

Figure 11. Start-up rotating speed of DSBSRM.

As shown in Figure 12, the start-up torques of DT/DSFC method and SOSM-DT/DSFC method reach steady state at 1 s and 0.5 s, respectively, which verifies the better torque dynamic response performance with SOSM-DT/DSFC method.

In order to study the output speed chattering and accuracy problems, the motor speed is stabilized at rated speed of 2500 r/min. Figure 13 shows an enlarged view of the steady-state speed waveform

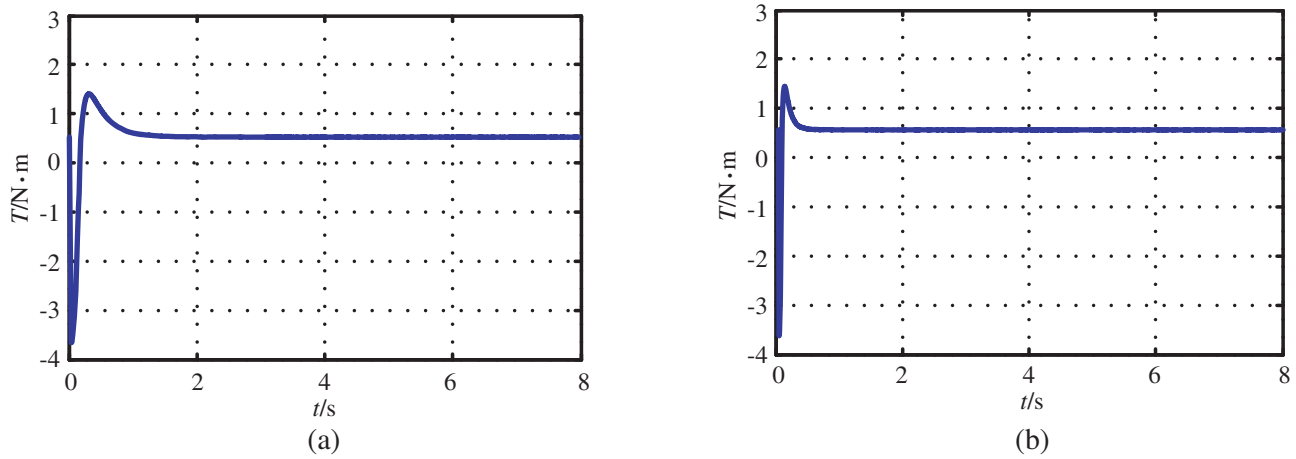

Figure 12. Start-up torque of DSBSRM. (a) DT/DSFC. (b) SOSM-DT/DSFC.

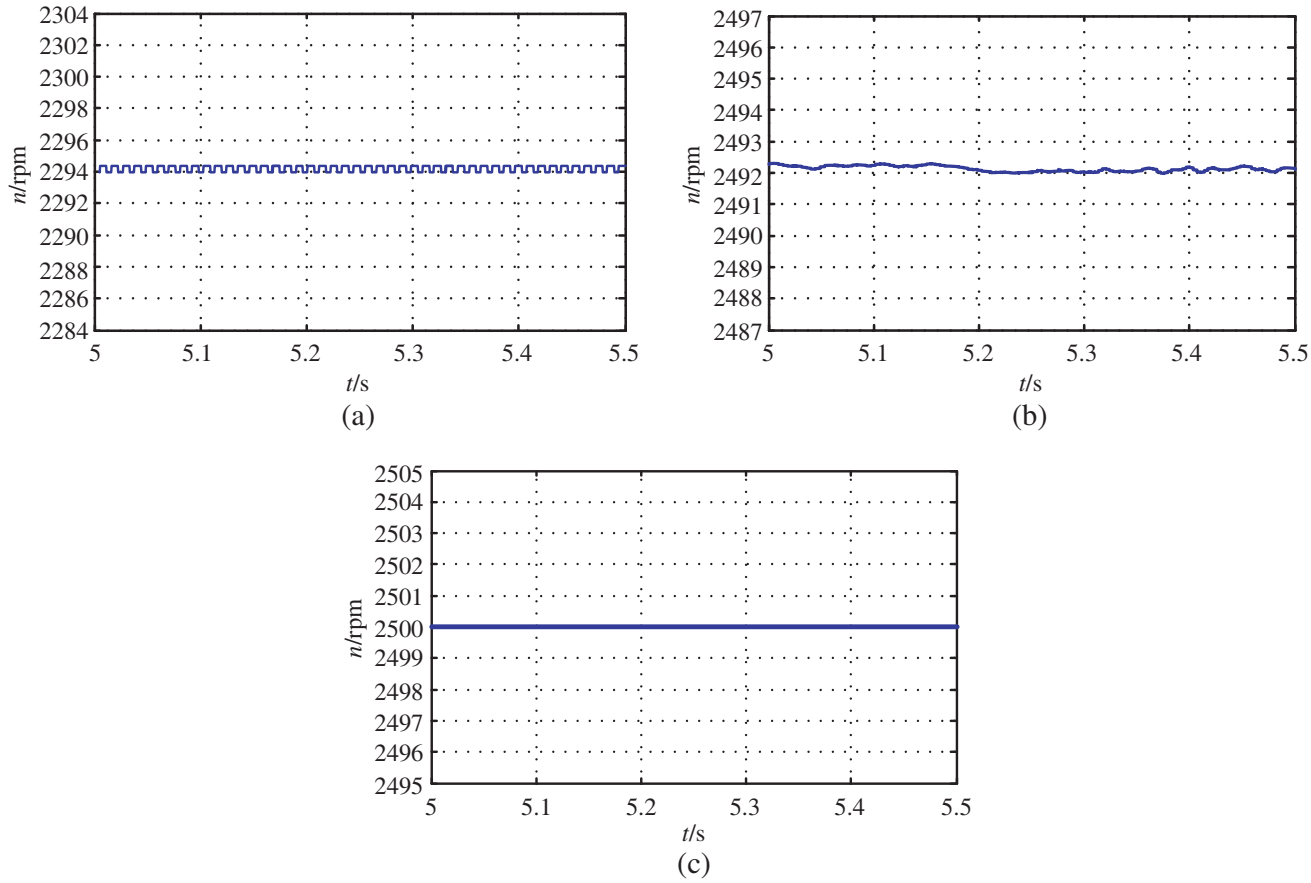

Figure 13. Steady speed of DSBSRM. (a) Traditional square wave control. (b) DT/DSFC. (c) SOSM-DT/DSFC.

with different control methods of DSBSRM. Figure 13(a) shows the steady-state speed waveform of the traditional square wave control. The speed is stable at 2294 r/min approximately; the speed fluctuation amplitude is 0.5 r/min; and the target speed has a maximum speed error of 206 r/min. Figure 13(b) shows that the speed is stable at 2492 r/min approximately; the speed fluctuation amplitude is 0.3 r/min;

and the maximum speed error is 8 r/min. As shown in Figure 13(c), there is almost no speed chattering and error with SOSM-DT/DSFC. Therefore, the speed fluctuation and speed error are reduced greatly by DT/DSFC method compared with the traditional square wave method. SOSM-DT/DSFC further reduces speed fluctuations and errors based on DT/DSFC, virtually eliminating speed chattering and error.

In order to verify the robustness of SOSM-DT/DSFC method, when the speed is stable at rated speed of 2500 r/min, external disturbance is applied to the motor, and the load torque changes from 0.3 N·m to 0.4 N·m at 5 s. The speed and torque waveforms are analyzed with different control methods of DSBSRM.

As shown in Figure 14(b), under abrupt load change using DT/DSFC, the speed waveform has changed significantly at 5 s. The maximum speed error is 30 r/min approximately, and it returns to the target speed at 7 s. As shown in Figure 15(b), under abrupt load change using SOSM-DT/DSFC, the speed waveform has changed slightly at 5 s. The maximum speed error is 2 r/min approximately, and it returns to the target speed at 5.2 s. Comparing Figure 14 and Figure 15, when the load torque is abrupt, the SOSM-DT/DSFC has a smaller change in speed than the DT/DSFC, and the torque subsystem is more robust.

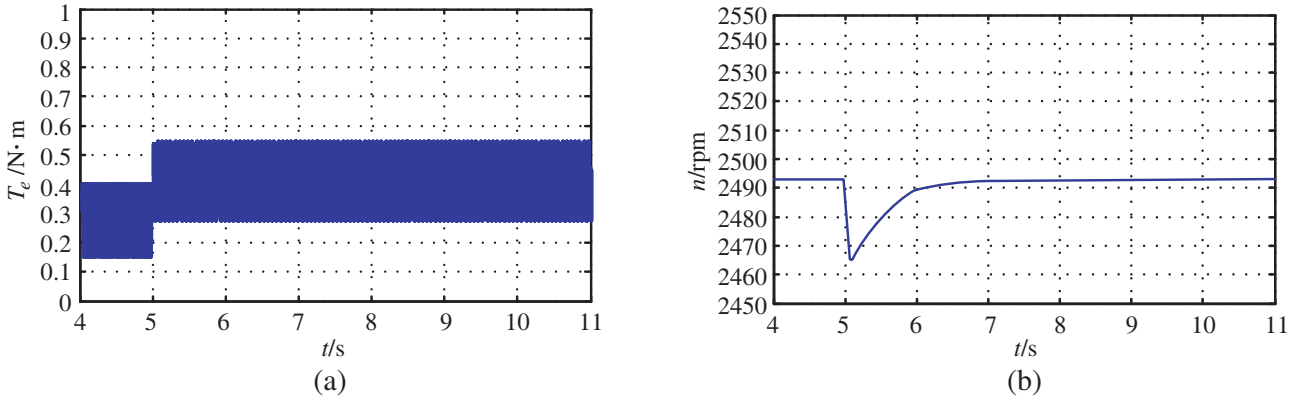

Figure 14. Results under abrupt load change using DT/DSFC. (a) Torque waveform. (b) Speed waveform.

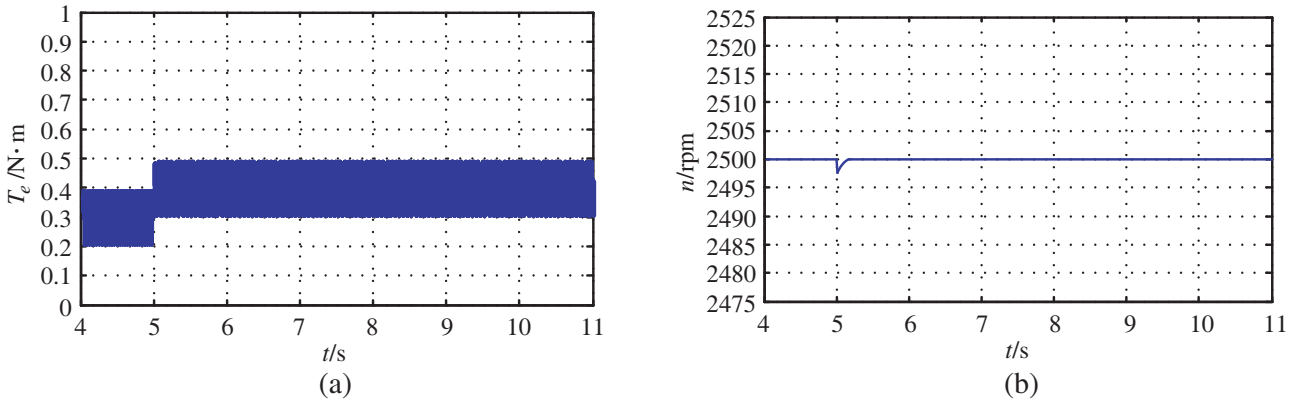

Figure 15. Results under abrupt load change using SOSM-DT/DSFC. (a) Torque waveform. (b) Speed waveform.

5. CONCLUSION

This paper introduces the structure and mathematical model of DSBSRM. Due to its decoupling characteristic between torque windings and suspension force windings, the torque subsystem and suspension force subsystem of DSBSRM can be controlled separately. In order to achieve the suppression of the torque ripple and improve the dynamic performance and robustness of speed, a DTC strategy using SOSM speed controller is proposed through referring to DTC strategy of conventional SRM. In order to achieve the suppression of the suspension force ripple and rotor displacement chattering, a DSFC strategy is proposed as well. Then the SOSM-DT/DSFC model is established by simulink. The results show that the proposed control strategy can effectively reduce the torque and suspension force ripple, and improve the dynamic performance and robustness of the system.

REFERENCES

1. Chiba, A., K. Kiyota, N. Hoshi, M. Takemoto, and S. Ogasawara, "Development of a rare-earth-free SR motor with high torque density for hybrid vehicles," *IEEE Transactions on Energy Conversion*, Vol. 30, No. 1, 175–182, Mar. 2015.
2. Rahman, K. M., B. Fahimi, G. Suresh, A. V. Rajarathnam, and M. Ehsani, "Advantages of switched reluctance motor applications to EV and HEV: Design and control issues," *IEEE Transactions on Industry Applications*, Vol. 36, No. 1, 111–121, Jan.–Feb. 2000.
3. Yang, Z., F. Shang, I. P. Brown, and M. Krishnamurthy, "Comparative study of interior permanent magnet, induction, and switched reluctance motor drives for EV and HEV applications," *IEEE Transactions on Transportation Electrification*, Vol. 1, No. 3, 245–254, Oct. 2015.
4. Chiba, A., et al., "Torque density and efficiency improvements of a switched reluctance motor without rare-earth material for hybrid vehicles," *IEEE Transactions on Industry Applications*, Vol. 47, No. 3, 1240–1246, May–Jun. 2011.
5. Krishnamurthy, M., C. S. Edrington, A. Emadi, P. Asadi, M. Ehsani, and B. Fahimi, "Making the case for applications of switched reluctance motor technology in automotive products," *IEEE Transactions on Power Electronics*, Vol. 21, No. 3, 659–675, May 2006.
6. Takemoto, M., H. Suzuki, A. Chiba, T. Fukao, and M. A. Rahman, "Improved analysis of a bearingless switched reluctance motor," *IEEE Transactions on Industry Applications*, Vol. 37, No. 1, 26–34, Jan.–Feb. 2001.
7. Sun, Y., Y. Yuan, and Y. Huang, "Design and analysis of bearingless flywheel motor specially for flywheel energy storage," *Electronics Letters*, Vol. 52, No. 1, 66–68, 2016.
8. Takemoto, M., A. Chiba, H. Akagi, et al., "Radial force and torque of a bearingless switched reluctance motor operating in a region of magnetic saturation," *IEEE Transactions on Industry Applications*, Vol. 40, No. 1, 103–112, 2004.
9. Chen, L. and W. Hofmann, "Design procedure of bearingless high-speed switched reluctance motors," *2010 International Symposium on Power Electronics Electrical Drives Automation and Motion (SPEEDAM)*, IEEE, 2010.
10. Wang, et al., "Design of novel bearingless switched reluctance motor," *IET Electric Power Applications*, Vol. 6, No. 2, 73, 2012.
11. Xu, Z., "Design and analysis of a novel 12/14 hybrid pole type bearingless switched reluctance motor," *IEEE International Symposium on Industrial Electronics*, IEEE, 2012.
12. Yang, Y., F. Liu, and C. Liu, "A new bearingless switched reluctance motor with wide rotor pole arc," *Industrial Electronics & Applications*, 2014.
13. Wei, P., et al., "Design and characteristic analysis of a novel bearingless SRM with double stator," *IEEE International Symposium on Industrial Electronics*, 2012.
14. Reddy, P. K., D. Ronanki, and P. Parthiban, "Direct torque and flux control of switched reluctance motor with enhanced torque per ampere ratio and torque ripple reduction," *Electronics Letters*, Vol. 55, No. 8, 477–478, Apr. 18, 2019.

15. Cao, X., J. Zhou, C. Liu, and Z. Deng, "Advanced control method for a single-winding bearinglessswitched reluctance motor to reduce torque ripple and radial displacement," *IEEE Transactions on Energy Conversion*, Vol. 32, No. 4, 1533–1543, Dec. 2017.
16. Takahashi, I. and Y. Ohmori, "High-performance direct torque control of an induction motor," *IEEE Transactions on Industry Applications*, Vol. 25, No. 2, 257–264, Mar.–Apr. 1989.
17. Cheok, A. D., "A new torque and flux control method for switched reluctance motor drives," *IEEE Trans. Power Electronics*, Vol. 17, No. 4, 543–557, 2002.
18. Takemoto, M., A. Chiba, and T. Fukao, "A method of determining the advanced angle of square-wave currents in a bearingless switched reluctance motor," *IEEE Transactions on Industry Applications*, Vol. 37, No. 6, 1702–1709, Nov.–Dec. 2001.
19. Xu, Z., D. Lee, and J. Ahn, "Comparative analysis of bearinglessswitched reluctance motors with decoupled suspending force control," *IEEE Transactions on Industry Applications*, Vol. 51, No. 1, 733–743, Jan.–Feb. 2015.
20. Cao, X., Z. Deng, G. Yang, and X. Wang, "Independent control of average torque and radial force in bearinglesss witched-reluctance motors with hybrid excitations," *IEEE Transactions on Power Electronics*, Vol. 24, No. 5, 1376–1385, May 2009.
21. Wu, X., Y. Yang, and Z. Liu, "Analysis and control of a novel bearingless switched reluctance motor with wider rotor teeth," *IECON 2017 — 43rd Annual Conference of the IEEE Industrial Electronics Society*, 1796–1801, Beijing, 2017.
22. Ammar, A., A. Bourek, and A. Benakcha, "Nonlinear SVM-DTC for induction motor drive using input-output feedback linearization and high order sliding mode control," *ISA Transactions*, Vol. 67, 428–442, 2017.
23. Huangfu, Y.-G., et al., "Chattering avoidance high order sliding mode control for permanent magnet synchronous motor," *Electric Machines and Control*, 2012.
24. Rafiq, M., et al., "A second order sliding mode control design of a switched reluctance motor using super twisting algorithm," *Simulation Modelling Practice and Theory*, Vol. 25, 106–117, 2012.
25. Ro, H., H. Jeong, and K. Lee, "Torque ripple minimization of switched reluctance motor using direct torque control based on sliding mode control," *2013 IEEE International Symposium on Industrial Electronics*, 1–6, Taipei, 2013.